MDPI

Article

Formation of Metallic Ag on AgBr by Femtosecond Laser Irradiation

Luís Cabral [1], Juan Andrés [2,*], Elson Longo [3], Miguel A. San-Miguel [4] and **Edison Z. da Silva [1,*]**

1   Institute of Physics "Gleb Wataghin" (IFGW), State University of Campinas, Campinas 13083-859, Brazil; lcabral@ifi.unicamp.br
2   Department of Inorganic and Organic Chemistry, University Jaume I (UJI), 12071 Castelló, Spain
3   LIEC-CDMF, Department of Chemistry, Federal University of São Carlos, São Carlos 13565-905, Brazil; elson.liec@gmail.com
4   Institute of Chemistry, State University of Campinas, Campinas 13083-970, Brazil; smiguel@unicamp.br
*   Correspondence: andres@qfa.uji.es (J.A.); zacarias@ifi.unicamp.br (E.Z.d.S.)

Abstract: Laser irradiation of materials induces changes in their structure and functional properties. In this work, lattice heating and electronic excitation on silver bromide (AgBr), provoked by femtosecond laser irradiation, have been investigated by finite-temperature density functional theory and *ab initio* molecular dynamics calculations by using the two-temperature model. According to our results, the electronic temperature of 0.25 eV is enough to excite the electrons from the valence to the conduction band, whereas 1.00 eV changes the structural properties of the irradiated AgBr material. Charge density simulations also show that an Ag clustering process and the formation of Br_3^- complexes take place when the electronic temperature reaches 2.00 eV and 5.00 eV, respectively. The present results can be used to obtain coherent control of the extreme nonequilibrium conditions due to femtosecond laser irradiation for designing new functional materials.

Keywords: finite temperature-density functional theory; *ab initio* molecular dynamics; two-temperature model; femtosecond laser irradiation; AgBr; clustering process

1. Introduction

Femtosecond laser irradiation (FLI) on semiconductor structures has attracted the attention of the scientific community due to its ability to produce and functionalize new materials by engineering their structure, and the electronic and optical properties [1–4], with applications in medicine and the electronic industry [5–7]. FLI induces structural changes and electronic excitation on the irradiated material [8]. The high kinetic energy of the excited atoms leads to the loss of crystallinity and the irradiated material tends to transform into amorphous [9]. Amorphous regions present a high degree of structural disorganization. Under the effect of FLI, both reduction and oxidation processes are expected, forming metallic clusters constituted by reduced species in specific lattice regions [10]. However, understanding how these chemical and physical processes occur and their nature remains a challenge.

Previously, FLI-based techniques have been employed in different applications, such as nonlinear lithography [11], the crystallization of amorphous semiconductors [12], and the increase in the performance of microsuper capacitors [13], as well as to improve the functionalities of existing materials [14] and to perform intelligent real-time control of pulses [15]. These experimental results boost theoretical studies based on real-time *ab initio* calculations [16]. Due to mass and charge differences between the electrons and nuclei, the FLI first provides a faster electronic response and an immediate electron excitation. As the energy of the laser pulses is higher than the band gap of materials, the closest electrons from the Fermi energy populate the empty levels of the conduction band (CB). Increasing the electronic temperature, electrons from the inner levels of the valence band (VB) will also

be excited. The energy relaxation channels for the ground state include electron-electron collision, phonon dispersion, and electron-phonon coupling.

Complex processes involving FLI on materials can be investigated by employing different theoretical methods, such as finite-temperature density functional theory (FT-DFT), in which the smearing methods for Brillouin zone integration within the electronic temperature (T_e) approach are used to simulate the laser effects caused by electronic excitation [17]. As intense laser irradiation provides heat to the material lattice, *ab initio* molecular dynamics (AIMD) simulations can be employed to understand the ionic temperature (T_i) effects induced by laser incidence. Thus, FT-DFT and AIMD methods are combined using the two-temperature model (TTM). This model was proposed by Alavi et al. [18] to elucidate the irradiation effects on hot hydrogen atoms. A few years later, Silvestrelli et al. reported their studies of lattice heat, melting point, and chemical bonds for silicon [19,20]. In a previous study, we also reported the use of the TTM to understand the electronic excitation in InP [21]. Recently, phonon dispersion and phonon–phonon coupling were calculated by using the TTM to understand the heat transfer and thermal conductivity in graphene [22].

Our research group is engaged in a project focused on understanding the effects of FLI on Ag-based compounds through the interplay between advanced experimental measurements and accurate computational simulations at the atomic level within density functional theory. We have reported the formation of Ag nanoparticles on the surface of silver tungstate, α-Ag$_2$WO$_4$, assisted by FLI, where the bactericidal and antiviral activity of these materials were discovered and extensively studied [23]. Additionally, we addressed the formation of In nanoparticles on the surface of irradiated indium phosphide (InP) [24], the formation of AgBi nanoalloys by FLI [25], and a theoretical report on the miscibility of Ag and Bi atoms to form AgBi nanoalloys [26]. Very recently, we obtained the formation of a heterojunction between Ag$_2$CrO$_4$ and Bi$_2$O$_3$ by FLI [27]. These studies allowed us to disclose the breaking/forming processes of the corresponding chemical bonds associated with the changes in the structure and properties of the irradiated materials.

Silver bromide (AgBr) is a semiconductor with a zinc blend structure (cubic face-centered unit-cell) and a direct forbidden energy region with a wide range of technological applications: transport and conductivity [28], environmental [29], energy treatment [30], photocatalytic [7] and antimicrobial [31] activities. In this work, using the FT-DFT and TTM models, the effects of both electronic excitation and lattice heating induced by FLI on AgBr, a representative semiconductor material, were investigated in detail. This paper is organized as follows: first, Section 2 reports the computational details and theoretical approach used to obtain the results presented in Section 3, where Section 3.1 discusses the limit for electronic excitation, and Section 3.2 elucidates the formation of metallic Ag clusters. Section 3.3 describes the electron density distributions using topological Bader charge analysis and the changes in the chemical environment due to femtosecond laser excitation. Finally, our main conclusions are presented in Section 4.

2. Theoretical Approach and Computational Details

FT-DFT and AIMD calculations were carried out using the generalized gradient approximation with the exchange correlation energy functional as proposed by Perdew–Burke–Erzenhof (PBE) [32]. The projector augmented-wave (PAW) method was used to describe the electron–ion interactions [33,34], as implemented in the Vienna *ab initio* simulation package (VASP) [35], version 6.2.1, where the following PAW valence states $4d^{10}$, $5s^1$ and $4s^2$, $4p^5$ for Ag and Br were employed, respectively. The equilibrium geometries for AgBr were obtained by stress-tensor minimization with a plane wave expansion cutoff of 500 eV, while the force optimization cutoff was 281 eV, which is 12.5% larger than the cutoff energy recommended by the VASP package. The difference between the stress tensor and the atomic forces calculation is the number of plane waves, increasing (decreasing) the computational cost with the higher (smaller) number of plane waves used.

To project the maximally localized Wannier functions (MLWF), the Wannier90 code was used, as implemented by Marzari and Vanderbilt [36]. In these calculations, the inter-

polated band structure was compared with DFT calculations. For the radial distribution function (RDF), the Pymatgen (Python Materials Genomics) code was employed [37], which is an open-source Python library for materials analysis. In our molecular dynamics investigations, the mean square displacement (MSD) was computed through the VASPKIT code [38], version 1.2.5. Additionally, the Phonopy code, version 2.11, allowed us to investigate the phonon dispersion along the high-symmetry q-points by using the atomic forces displacement and the force constants calculations [39].

To simulate the FLI, T_e within the FT-DFT approach was employed using a Gaussian-like function for the Brillouin zone smearing [40].

$$f\left(\frac{\varepsilon - \mu}{\sigma}\right) = \frac{1}{2}\left(1 - erf\left[\frac{\varepsilon - \mu}{\sigma}\right]\right)$$

where ε, μ, and $\sigma = K_B T_e$ are the energy band, chemical potential, and the smearing method, written as a function of the Boltzmann constant and electronic temperature, as implemented in the VASP package. In our calculations, a low electronic temperature of $T_e = 0.01$ eV was used to minimize the stress tensor and obtain the equilibrium volume of AgBr, and after that, the width of the Brillouin zone integration was varied from $T_e = 0.01$ eV until 6.00 eV, fixing the AgBr lattice parameter.

The TTM was adopted using AIMD simulations and the FT-DFT approach [18,40–42]. In these calculations, a supercell was built from the primitive unit cell multiplied by two in the three space directions (resulting in 32 Ag and 32 Br atoms). Only a reduced gamma-point was used for the Brillouin zone integration to minimize the computational efforts. The microcanonical ensemble (NVE) was adopted, the time step in the integration of the equations of motion was 0.5 fs, and simulations spanned for 5.0 ps.

For the calculation of the structural and vibrational properties, a $6 \times 6 \times 6$ k-mesh was used for the Brillouin zone integration and $12 \times 12 \times 12$ for the electronic and charge calculations using a Gaussian smearing method. In addition, the electronic convergence criterion was 10^{-6} eV, and the atoms were allowed to relax until all forces were smaller than 10^{-2} eV·A^{-1} on every atom.

3. Results

The mechanical and electronic properties of AgBr in the zinc-blend bulk phase were investigated within the FT-DFT approach to elucidate the faster electron response to laser irradiation. Furthermore, *ab initio* molecular dynamics simulations were carried out to investigate the effects on the slower excited ion response and the initial diffusion processes.

3.1. FT-DFT Investigation: Limits for Electronic Excitation

To ensure that the choice of the convergence criteria to solve the Kohn-Sham scheme are satisfied for a given k-mesh, $T_e \to 0$ was adopted. Smaller electronic temperatures are generally used to avoid partial occupations of electronic states near the Fermi energy. However, within the *ab initio* DFT calculations, a very small T_e provides the discontinuity of the Brillouin zone integration, and therefore, T_e must be tested for each particular system. Here, $T_e = 0.01$ eV was used to obtain the ground state properties.

The converged lattice parameter for AgBr was 6.30 Å, which is in good agreement with the reported value of 6.33 Å [43], with a deviation of only 0.03 Å (0.47%). The AgBr unit-cell has a cubic face-centered geometry with 4 Ag and 4 Br atoms, as represented in Figure 1. Additionally, the calculated band gap energy with PBE was 1.10 eV, also close to the experimental value of 1.17 eV [44], which is a direct band gap in the high symmetry Γ-point. These calculations show that the valence band maximum (VBM) is triply degenerated in the Γ-point corresponding to d_{xy}, d_{xz}, and d_{yz} Ag levels (t_{2g} states) and p_x, p_y, and p_z Br states.
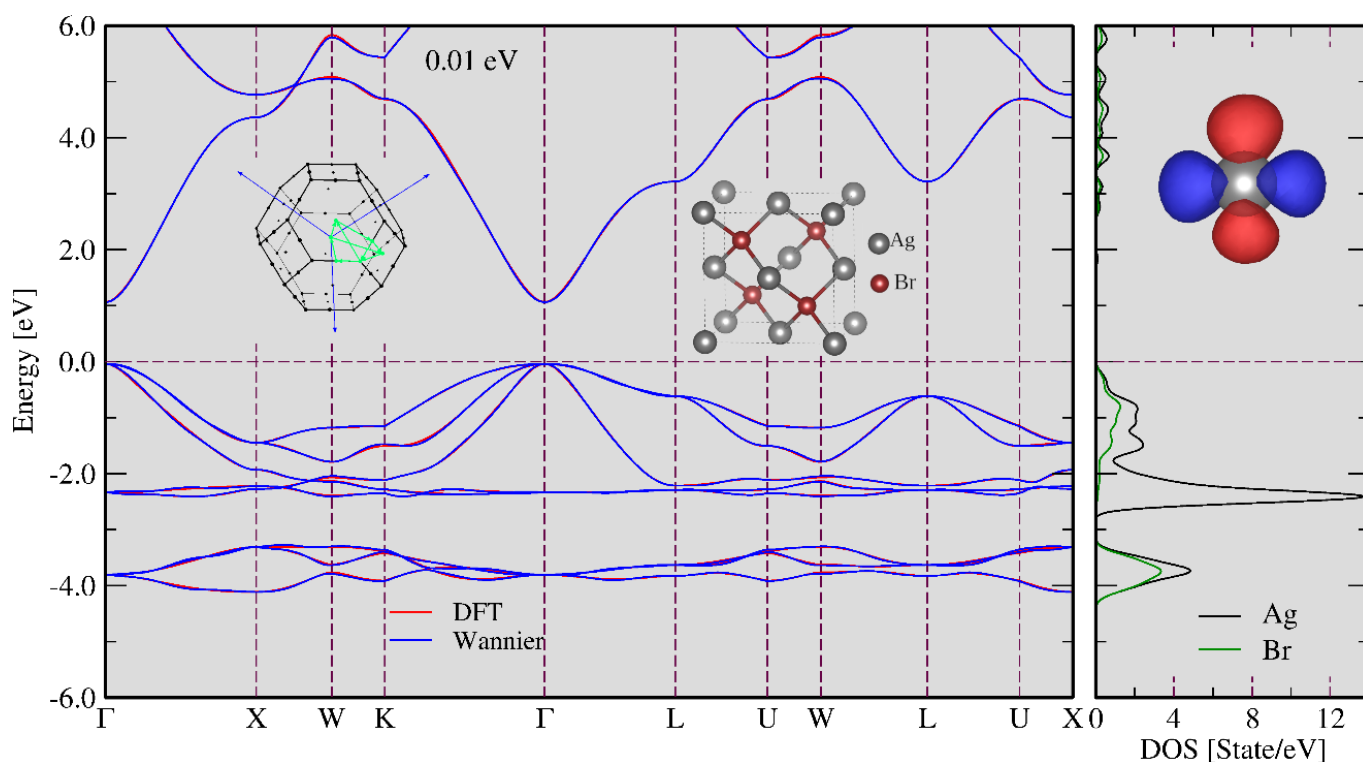
Figure 1. Electronic band structure for the AgBr unit cell, where the Ag and Br atoms are shown in silver and brown balls and the Brillouin zone (**left** panel). Summed electronic density of states (DOS) for AgBr and d-Ag Wannier orbitals (**right** panel).

The d_{z2} and d_{x2-y2} electronic levels (e_g-states) in the VBM are empty, and the conduction band minimum (CBM) only shows the nondegenerate s states. For $T_e = 0.01$ eV, the electrons in the VBM preferably occupy the d_{xy}-Ag state and the p_x and p_y Br states. The CBM is only composed of s-Ag and s-Br states. Figure 1 displays the agreement between the electronic band structure obtained by DFT and Wannier interpolation, the high symmetry points of the Brillouin zone calculation, the Wannier d-Ag orbitals, and the summed electronic density of states.

FT-DFT was employed to understand the electronic excitation due to femtosecond laser irradiation. In these investigations, comparative calculations increasing T_e were performed to obtain the structural parameters of the AgBr lattice converged at $T_e = 0.01$ eV. Analyzing the electron density distribution at $T_e = 0.25$ eV shows that electrons are already in the conduction band. This phenomenon becomes more evident for $T_e = 0.75$ eV, which varies the electronic chemical potential and, consequently, the chemical environment of the AgBr semiconductor. In addition, an increase in the electronic entropy was observed at $T_e = 0.75$ eV, resulting in band gap shrinkage. However, for $T_e = 1.00$ eV, AgBr presents metallic characteristics, i.e., the Fermi energy and CBM are at close energy levels, the electronic occupation increases in the CBM, and the electrons begin to occupy higher levels of the conduction band. In addition, the electronic disorder increases significantly at $T_e = 1.00$ eV, indicating that this is a limit for the T_e approach for studying AgBr with semiconducting properties. As electronic disorder represents the energy difference between the total energy obtained with $T_e \rightarrow 0$ and the free energy; an increase in the DFT-total energy was observed when increasing the electronic excitation from $T_e > 1.00$ eV.

The occupation in the CBM increases until $T_e = 3.00$ eV and then decreases. Thus, $T_e = 3.00$ eV is our proposed limit for the electronic excitation on AgBr within the FT-DFT due to band structure stability in the presence of hot electrons. For $T_e > 3.00$ eV, the energy levels decrease with increasing T_e. More details of the band structure obtained by DFT calculations and Wannier interpolation for different electronic temperatures are reported in

Figure S1 of the Supplementary Materials (SM). Figure S2 of the Supplementary Materials represents the charge density for CBM, the next unoccupied state of the conduction band (CB), and the VBM levels as a function of the electronic temperature. For T_e = 0.01 eV, the major charge contributions in the VBM are given by the Ag atoms, while the Br atoms provide the electronic density in the CBM, and the CB is composed of the contributions of Ag atoms. By increasing the electronic temperature, the charge density in the electronic states changes, and AgBr loses its semiconductor properties at T_e = 1.00 eV. A charge transfer process between Ag and Br atoms at this electronic temperature is observed. For T_e > 2.00 eV, the charge density of the VBM, CBM, and CB in the AgBr ground state is mainly provided by Br. Then, the crystallinity and electronic conductivity are modified by the structural and electronic charges in the electronic states provoked by FLI. Figure S3 displays the increase (decrease) in the electron (hole) effective mass with the increase in T_e, denoting the possibility of engineering the transport properties of AgBr. Similarly, Figure S4 shows the calculation of the d-Ag band center as a function of the electronic excitation as a signature of how FLI can improve the photocatalytic activity of AgBr.

The structural stability of the zinc blend AgBr phase was investigated by calculating the elastic constants and the vibrational phonon dispersion as a function of T_e, as shown in Figures 2 and 3, respectively. The structural stability criteria for the cubic face-centered phase are met when the following elastic constants $C_{11} - C_{12} > 0$, $C_{11} + 2C_{12} > 0$, and $C_{44} > 0$ [45]. The increase in the electronic temperature from 0.01 eV up to 1.00 eV does not alter the structural properties, but for T_e > 1.00 eV, the elastic constants decrease smoothly until the system becomes unstable at T_e = 3.00 eV. The bulk ($B_0 = 1/3(C_{11} + 2C_{12})$) and shear ($S_0 = 1/2(C_{11} - C_{12})$) moduli also show the limit of T_e = 3.00 eV. This limit is also observed for phonon dispersion, where the phonon band structure remains practically the same in the range 0.01 eV < T_e < 1.00 eV; however, for T_e = 2.00 eV, some divergences appear in the acoustic modes, while for T_e = 3.00 eV, the acoustic modes become imaginary, demonstrating that the structure becomes unstable.
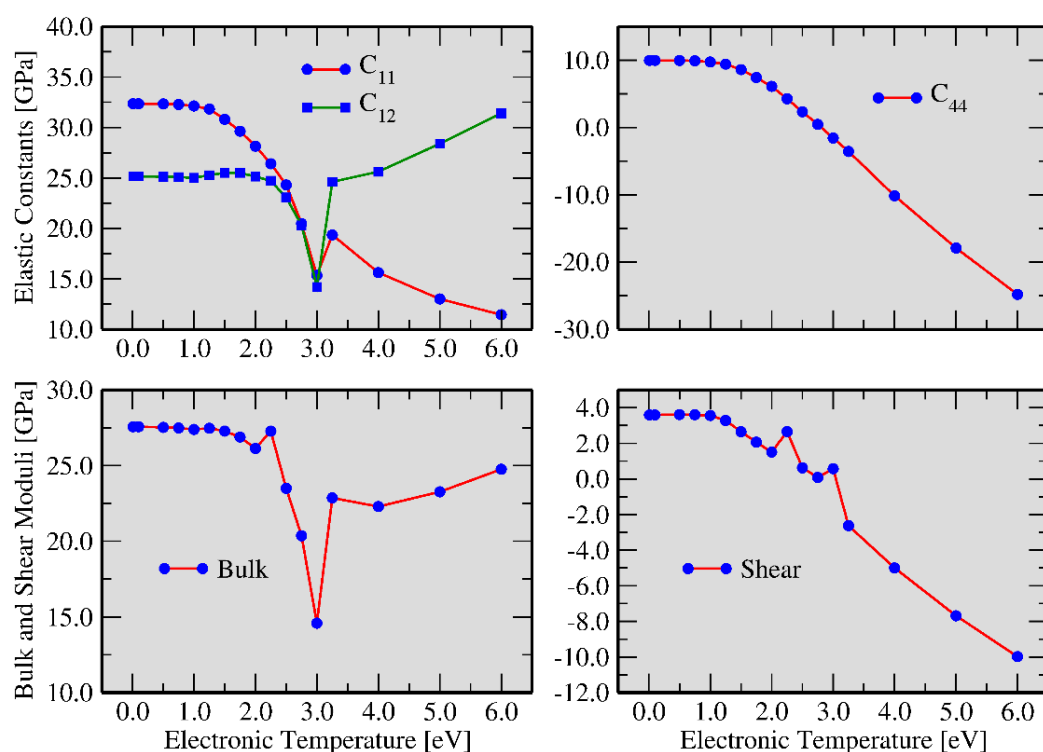

Figure 2. Calculated elastic constants (**top** panels), bulk and shear modulus (**bottom** panels) as a function of the electronic temperature. The C_{11}, C_{12} and C_{44} elastic constants correspond to the AgBr-cubic face centered structure.
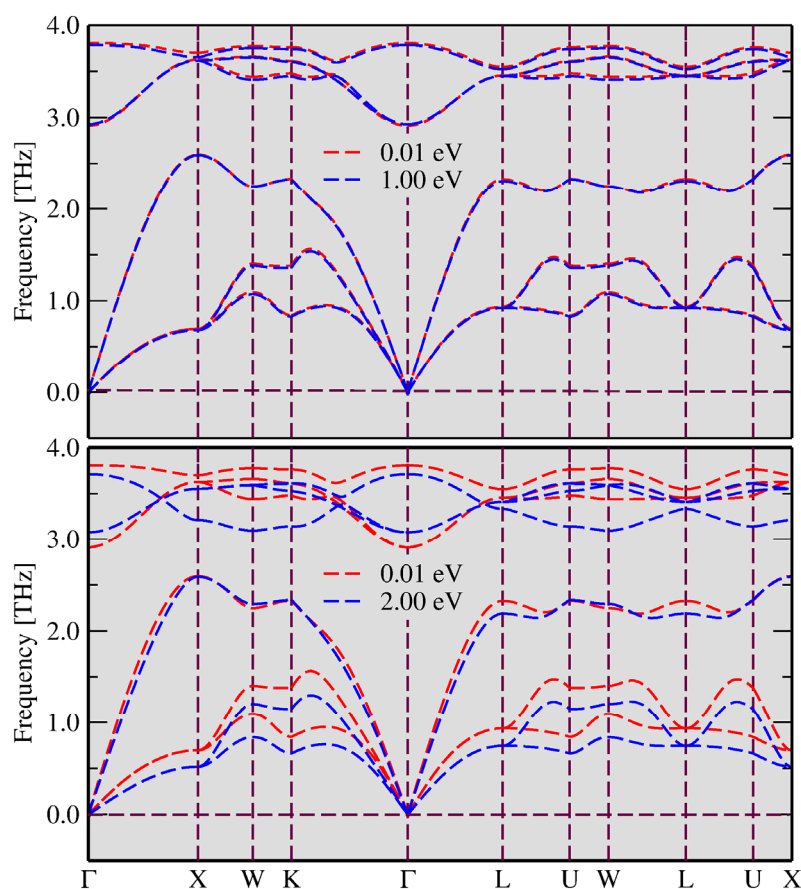
Figure 3. Phonon band structure for AgBr. The electronic temperature of $T_e = 0.01$ eV (red) was compared with $T_e = 1.00$ eV (blue, **upper** panel) and $T_e = 2.00$ eV (blue, **bottom** panel).

3.2. Two Temperature Model: Ab Initio Molecular Dynamics with Excited Atoms

An analysis of the results shows that until $T_e = 1.00$ eV, the increase in kinetic energy does not promote significant atomic displacements in the heated lattice. At higher T_e, in the first stage, the strong Coulomb repulsion between excited atoms, which shows expanded orbitals, causes the atoms to oscillate around their equilibrium positions. This effect introduces noncrystalline areas and decreases the overlap region between the Ag and Br atoms. However, new energy levels may be generated within the band gap. This is the starting point for symmetry breaking, causing polarization of the AgBr structure. In this way, the system that was polarized at short and medium ranges produces a long-range polarization. This fact leads to a significant structural rearrangement, with the formation of new absorption centers of photons and the creation of metallic Ag. In the second stage, there are mobile electrons in the CB and holes in the VB. Due to the reduction of the Ag cations and the oxidation of the Br anions, AgBr, which is a semiconductor at low electronic temperatures, evolves to metallic behavior. At this stage, clusters of Ag and Br atoms are formed. Geometrical alterations in these clusters, such as distortions, breathing, and tilt, create a large variety of local structures associated with AgBr quasicrystals. In addition, an increase in the conductivity can be related to localized surface plasmon resonance effects producing metallic Ag.

At $T_e = 2.00$ eV, the Ag atoms tend to agglomerate in certain regions of the lattice, indicating the beginning of the Ag clustering process. The simulation time for AgBr was extended to 10.0 ps for an electronic excitation of 2.0 eV and the results obtained follow the same trends presented at 5.0 ps. Higher electronic temperatures ($T_e > 2.00$ eV) accelerate the Ag clustering process in the heated lattice, removing the quasicrystallinity previously obtained with lower electronic temperatures and turning it into an amorphous solid. In the silver diffusion process, the Ag clusters formed present different types of symmetry, which

depend on the simulation time and the intensity of the electronic excitation. Due to the intensity of the laser, we can infer that the Br_2 molecules evaporate after the beginning of the Ag clustering and, after intense laser irradiation, Br_3^- species are formed [46]. The laser-induced fluorescence properties of Br_2 were investigated in Ref. [47]. Figure 4 illustrates snapshots from the simulations at different electronic temperatures, where Ag clustering regions and Br_3^- complexes are depicted at $T_e = 2.00$ eV.
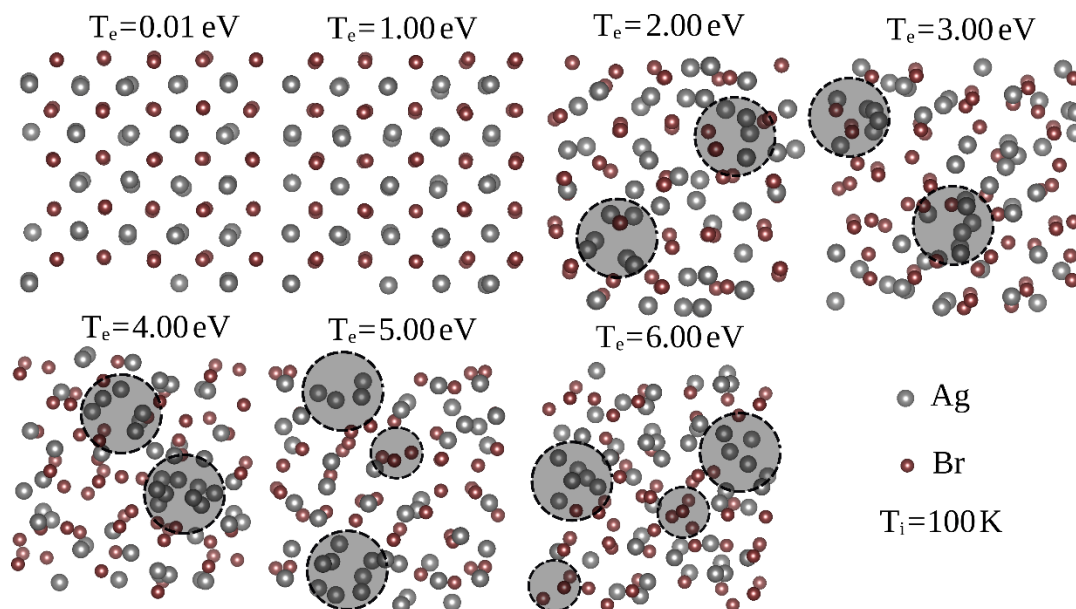

Figure 4. Two-temperature model calculations to simulate the FLI. The Ag and Br atoms are depicted in silver and brown colors, while their clusters are represented by gray circles.

In an analysis of the random distribution of the formed clusters of Ag and Br, the cluster sizes increase as the electronic temperature increases. Additionally, the shape, geometry, and symmetry of the formed clusters vary as a function of the irradiation time and T_e. These, in turn, connect to each other to form superclusters with low symmetry. Furthermore, for $T_e = 5.00$ eV and $T_e = 6.00$ eV, the system exhibits a high degree of disorder typical of amorphous materials.

Figure 5 displays the evolution of the values of T_i as a function of time for the applied T_e. The different electronic temperatures used in each simulation result in different kinetic energies for the atoms and, consequently, different lattice temperatures. At the lowest T_e (1.00 eV), the lattice is lightly heated, and atoms stay at equilibrium positions. However, at 2.00 eV, the lattice temperature is still low (ca. 170 K); however, significant structural changes occur. A significant increase in the lattice temperature was observed at 3.00 eV and 4.00 eV, namely, 600 K and 1660 K, respectively.

To investigate the structural arrangements, the radial distribution functions (RDFs) were computed at different electronic temperatures after 5.00 ps of simulation, and they are depicted in Figure 6. For lower electronic temperatures up to 1.00 eV, the peaks for the Ag-Ag distances are approximately equally distributed, as expected from a crystalline structure. For $T_e = 2.00$ eV, a single and well-defined Ag-Ag peak emerges at 2.8 Å, indicating the formation of small Ag clusters. At this temperature, the Br-Br profile loses the characteristic crystalline behavior, and the shortest Br-Br distances are approximately 3.5 Å. For higher temperatures, the distinct Ag-Ag peak is slightly shifted to 3.0 Å and increases, reflecting certain growth in the formed Ag clusters. Additionally, the appearance of Br-Br distances at 2.28 Å confirms the formation of Br_3^- species [47]. Additional simulations at $T_e = 2.00$ eV with initial system temperatures set to 10 K, 100 K, and 300 K were conducted. Figure S5 depicts the corresponding RDFs showing similar features and demonstrating

that the structural rearrangements produced at T_e = 2.00 eV are a consequence of electronic excitation and are not caused by the kinetic energy associated with the lattice temperature.
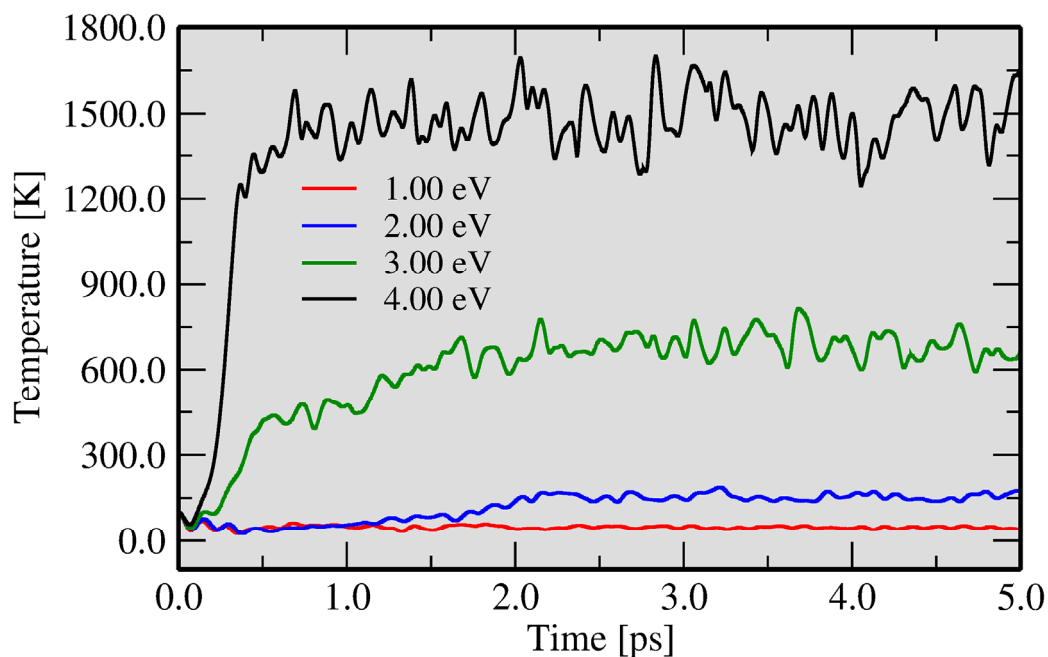

Figure 5. *Ab initio* molecular dynamics with the excited atoms: temperature evolution as a function of time for calculated electronic temperatures of 1.00 eV (red), 2.00 eV (blue), 3.00 eV (green) and 4.00 eV (black).
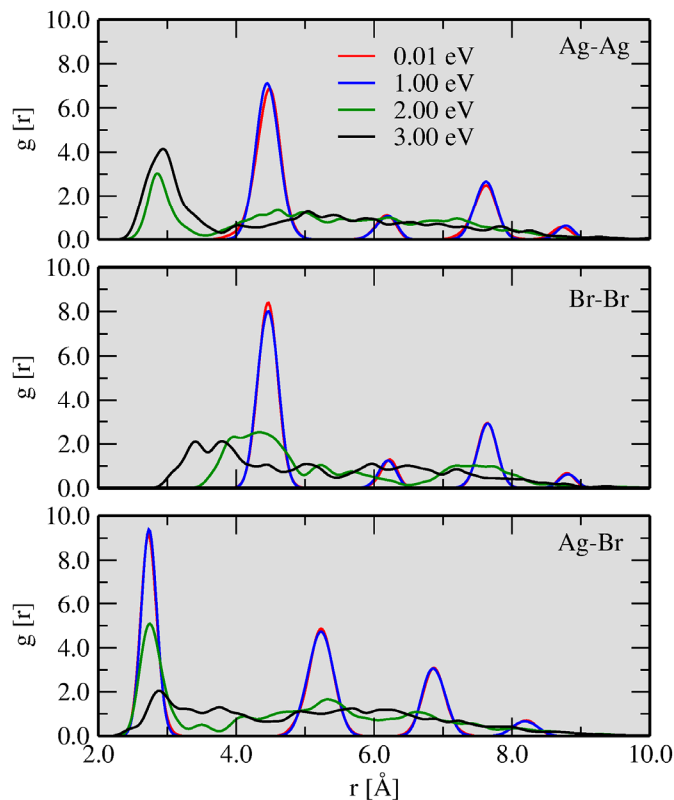

Figure 6. Radial distribution function for the geometries shown in Figure 4. In the top, center and bottom panels, the radial distribution function is calculated for Ag-Ag, Br-Br and AgBr, respectively, as a function of the electronic temperature.

Furthermore, the diffusion processes induced by the laser irradiation were monitored by computing the MSD, as depicted in Figure 7. For low electronic temperatures (T_e < 1.00 eV), the MSD for both Ag and Br atoms present small values, indicating that they oscillate around their equilibrium positions. However, as mentioned before, at 2.00 eV, the electronic excitation is enough to promote the diffusion of both atom species, with higher mobility for Ag and allowing the consequent formation of Ag clusters. For excitation at 3.00 eV, the MSD slopes are pronounced and similar for both Ag and Br, indicating the loss of crystalline structure and enhancing the growth of the Ag clusters and the formation of Br_3^- species.
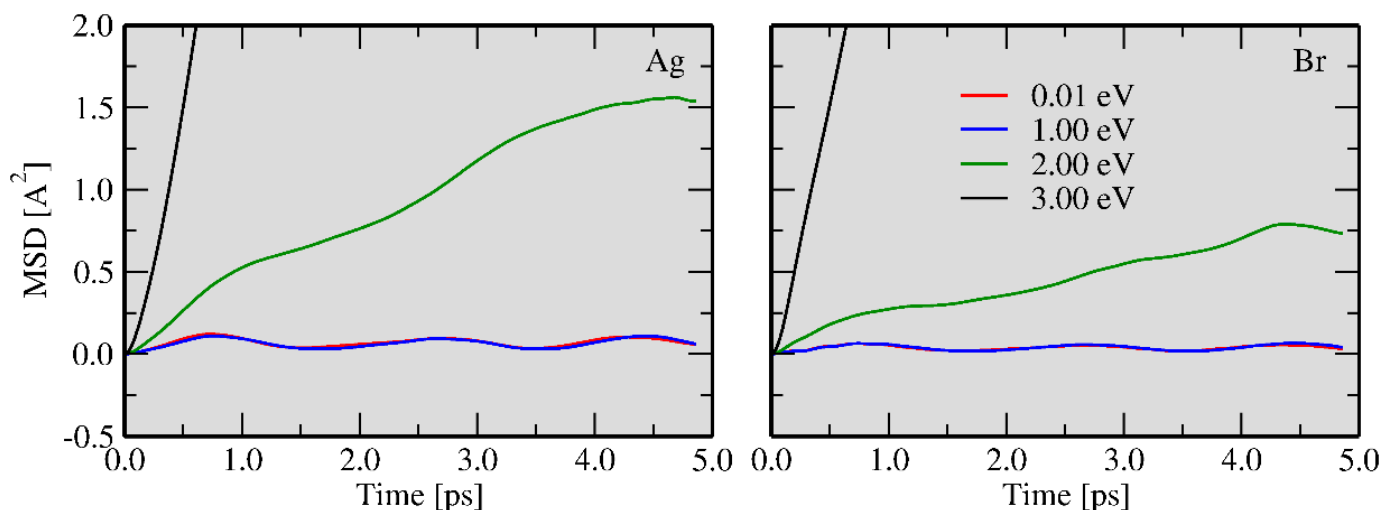

Figure 7. Mean square displacement for Ag (**left** panel) and Br (**right** panel) as a function of the electronic temperature.

3.3. Ag and Br Clustering Processes: Charge Flow

The analysis of the effective Bader charges allows us to investigate the charge transfer processes and understand the attractive or repulsive Coulomb interactions between the atoms during the diffusion mechanisms, leading to the formation of metallic clusters. Figure 8 depicts the calculated effective Bader charges for each T_e. The effective Bader charge (Q_{eff}^B) (in |e| units) is given by the difference between the number of valence electrons (Z_{val}) and the calculated Bader (Q^{Bader}) charge, as $Q_{eff}^B = Z_{val} - Q^{Bader}$.
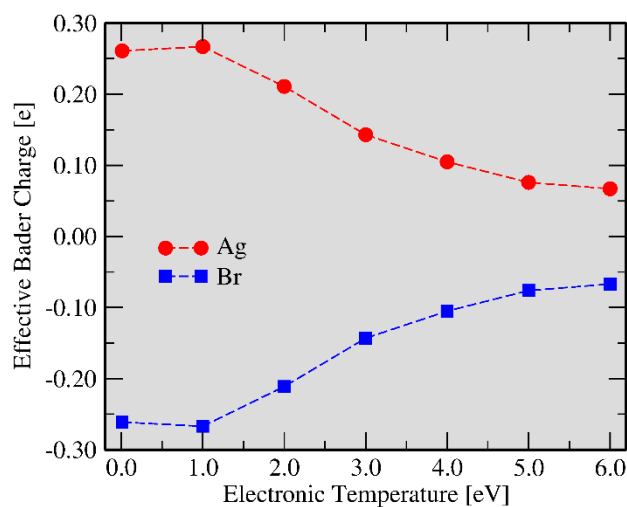

Figure 8. Effective Bader charge average calculation. The Ag (electropositive) atoms are represented in red, and Br (electronegative) atoms are represented in blue.

For T_e = 0.01 eV, after 5.00 ps of TTM simulations, as expected from the ionic nature of AgBr, the Ag atoms are positively charged (ca. + 0.25 |e|), whereas the Br species show negative charges. However, when the system is excited at 1.00 eV, the average charges still maintain similar behavior. At 2.00 eV, when diffusion processes of Ag atoms are initiated, the modulus of the average charges decreases, indicating the reduction and oxidation of Ag cations and Br anions, respectively. This process continues at the higher T_e investigated up to 6.00 eV, reflecting the formation of metallic Ag clusters, Br_2 molecules, and Br_3^- species.

4. Conclusions

The energy provided by FLI on AgBr in the zinc blend structure changes the structure and electronic properties under extreme nonequilibrium conditions. Both the FT-DFT and AIMD methods are employed using the two-temperature model (TTM). The AgBr equilibrium bulk volume and the band structure were simulated with the smaller T_e = 0.01 eV, and after that, total energy calculations were performed to study the electronic excitation. The main results of the present study can be summarized as follows: (i) the electronic properties are practically the same until T_e = 0.10 eV and the electrons begin to occupy the CBM for T_e = 0.25 eV; (ii) the structural and vibrational properties do not alter up to T_e = 1.00 eV, while for electronic excitation T_e = 3.00 eV, it was noted that the system becomes unstable; (iii) for smaller electronic temperatures than T_e = 1.00 eV, the atoms oscillate near their equilibrium positions, while for higher electronic excitation, the atomic displacements increased as a function of the T_e; (iv) for T_e = 2.00 eV, the kinetic energy of Ag, in comparison to Br, induces the formation process of Ag clusters and the subsequent diffusion process, while the Br atoms form Br_2 molecules and evaporate instantly; (v) the increase in T_e, favors the Ag clustering process; (vi) for T_e = 5.00 eV and T_e = 6.00 eV, the formation of Br_3^- complexes is observed; and (vii) RDF, MSD and electronic charge investigations for each electronic temperature confirm the appearance of the Ag clustering process, and the formation of Br complexes in specific regions of the material.

We hope that the present results contribute to the understanding and rationalization of the structural and electronic effects that FLI induces on materials and can be employed as a model for the rational design of new functional materials that can be applied in the microelectronics industry.

Author Contributions: Conceptualization, L.C. and M.A.S.-M.; methodology, L.C., M.A.S.-M. and J.A.; software, L.C.; validation, E.Z.d.S. and E.L.; formal analysis, L.C. and M.A.S.-M.; investigation, L.C.; resources, E.Z.d.S. and E.L.; data curation, L.C. and M.A.S.-M.; writing—original draft preparation, L.C., J.A., E.L. and E.Z.d.S.; writing—review and editing, L.C., J.A., E.L. and E.Z.d.S.; visualization, L.C., J.A., E.L. and E.Z.d.S.; supervision, E.Z.d.S. and E.L.; project administration, E.Z.d.S. and E.L.; funding acquisition, E.Z.d.S. All authors have read and agreed to the published version of the manuscript.

Institutional Review Board Statement: Not applicable.

Informed Consent Statement: Not applicable.

Data Availability Statement: The data presented in this study are available on request from the corresponding author.

Conflicts of Interest: The authors declare no conflict of interest. The funders had no role in the design of the study; in the collection, analyses, or interpretation of data; in the writing of the manuscript; or in the decision to publish the results.

References

1. Biasin, E.; Fox, Z.W.; Andersen, A.; Ledbetter, K.; Kjær, K.S.; Alonso-Mori, R.; Carlstad, J.M.; Chollet, M.; Gaynor, J.D.; Glownia, J.M.; et al. Direct observation of coherent femtosecond solvent reorganization coupled to intramolecular electron transfer. *Nat. Chem.* **2021**, *13*, 343–349. [CrossRef] [PubMed]
2. Jalil, S.A.; Lai, B.; ElKabbash, M.; Zhang, J.; Garcell, E.; Singh, S.; Guo, C. Spectral absorption control of femtosecond laser-treated metals and application in solar-thermal devices. *Light Sci. Appl.* **2020**, *9*, 14. [CrossRef]
3. Ludwig, M.; Aguirregabiria, G.; Ritzkowsky, F.; Rybka, T.; Marinica, D.C.; Aizpurua, J.; Borisov, A.G.; Leitenstorfer, A.; Brida, D. Sub-femtosecond electron transport in a nanoscale gap. *Nat. Phys.* **2019**, *16*, 341–345. [CrossRef]
4. Skopintsev, P.; Ehrenberg, D.; Weinert, T.; James, D.; Kar, R.K.; Johnson, P.J.M.; Ozerov, D.; Furrer, A.; Martiel, I.; Dworkowski, F.; et al. Femtosecond-to-millisecond structural changes in a light-driven sodium pump. *Nature* **2020**, *583*, 314–318. [CrossRef] [PubMed]
5. Luo, F.; Jiang, R.; Hu, X.; He, Z.; Wang, Y. Structure and properties of nano SiC coatings in-situ fabricated by laser irradiation. *Ceram. Int.* **2020**, *46*, 14747–14755. [CrossRef]
6. Momoki, K.; Manabe, T.; Li, L.; Yan, J. Silicon nanoparticle generation and deposition on glass from waste silicon powder by nanosecond pulsed laser irradiation. *Mater. Sci. Semicond. Process.* **2020**, *111*, 104998. [CrossRef]
7. Yang, H.; Cheng, J.; Liu, Z.; Liu, Q.; Zhao, L.; Wang, J.; Chen, M. Dynamic behavior modeling of laser-induced damage initiated by surface defects on KDP crystals under nanosecond laser irradiation. *Sci. Rep.* **2020**, *10*, 500. [CrossRef]
8. Sundaram, S.K.; Mazur, E. Inducing and probing non-thermal transitions in semiconductors using femtosecond laser pulses. *Nat. Mater.* **2020**, *1*, 217. [CrossRef]
9. Izawa, Y.; Izawa, Y.; Setsuhara, Y.; Hashida, M.; Fujita, M.; Sasaki, R.; Nagai, H.; Yoshida, M. Ultrathin amorphous Si layer formation by femtosecond laser pulse irradiation. *Appl. Phys. Lett.* **2007**, *90*, 044107. [CrossRef]
10. Shuleiko, D.V.; Potemkin, F.V.; Romanov, I.A.; Parhomenko, I.N.; Pavlikov, A.V.; Presnov, D.E.; Kashkarov, P.K. Femtosecond laser pulse modification of amorphous silicon films: Control of surface anisotropy. *Laser Phys. Lett.* **2018**, *15*, 056001. [CrossRef]
11. Öktem, B.; Pavlov, I.; Ilday, S.; Kalaycıoğlu, H.; Rybak, A.; Yavaş, S.; Ilday, F.Ö. Nonlinear laser lithography for indefinitely large-area nanostructuring with femtosecond pulses. *Nat. Photonics* **2013**, *7*, 897–901. [CrossRef]
12. Pan, C.-L.; Chen, K.-W.; Wang, Y.-C.; Kao, S.-H.; Wu, P. Room-temperature crystallization of amorphous silicon by near-UV femtosecond pulses. *AIP Adv.* **2020**, *10*, 055321. [CrossRef]
13. Xu, C.; Jiang, L.; Li, X.; Li, C.; Shao, C.; Zuo, P.; Liang, M.; Qu, L.; Cui, T. Miniaturized high-performance metallic 1T-Phase MoS2 micro-supercapacitors fabricated by temporally shaped femtosecond pulses. *Nano Energy* **2019**, *67*, 104260. [CrossRef]
14. Brahms, C.; Belli, F.; Travers, J.C. Infrared attosecond field transients and UV to IR few-femtosecond pulses generated by high-energy soliton self-compression. *Phys. Rev. Res.* **2020**, *2*, 043037. [CrossRef]
15. Pu, G.; Yi, L.; Zhang, L.; Luo, C.; Li, Z.; Hu, W. Intelligent control of mode-locked femtosecond pulses by time-stretch-assisted real-time spectral analysis. *Light Sci. Appl.* **2020**, *9*, 13. [CrossRef]
16. Nourbakhsh, Z.; Tancogne-Dejean, N.; Merdji, H.; Rubio, A. High Harmonics and Isolated Attosecond Pulses from MgO. *Phys. Rev. Appl.* **2021**, *15*, 014013. [CrossRef]
17. Zhao, S.; Zhang, Y.; Weber, W.J. Ab Initio Study of Electronic Excitation Effects on SrTiO$_3$. *J. Phys. Chem. C* **2017**, *121*, 26622–26628. [CrossRef]
18. Alavi, A.; Kohanoff, J.; Parrinello, M.; Frenkel, D. Ab Initio molecular dynamics with excited electrons. *Phys. Rev. Lett.* **1994**, *73*, 2599–2602. [CrossRef]
19. Silvestrelli, P.L.; Alavi, A.; Parrinello, M.; Frenkel, D. Ab initio molecular dynamics simulation of laser melting of silicon. *Phys. Rev. Lett.* **1996**, *77*, 3149–3152. [CrossRef]
20. Silvestrelli, P.L.; Alavi, A. Structural, dynamical, electronic, and bonding properties of laser-heated silicon: An ab initio molecular-dynamics study. *Phys. Rev. B Condens. Matter Mater. Phys.* **1997**, *56*, 3806–3812. [CrossRef]
21. Cabral, L.; Andrés, J.; Machado, T.R.; Picinin, A.; Rino, J.P.; Lopez-Richard, V.; Longo, E.; Gouveia, A.F.; Marques, G.E.; da Silva, E.Z.; et al. Evidence for the formation of metallic in after laser irradiation of InP. *J. Appl. Phys.* **2019**, *126*, 025902. [CrossRef]
22. An, M.; Song, Q.; Yu, X.; Meng, H.; Ma, D.; Baoling, H.; Jin, Z.; Huang, B.; Ruiyang, L. Generalized Two-Temperature Model for Coupled Phonons in Nanosized Graphene. *Nano Lett.* **2017**, *17*, 5805–5810. [CrossRef]
23. de Assis, M.; Robeldo, T.; Foggi, C.C.; Kubo, A.M.; Mínguez-Vega, G.; Condoncillo, E.; Beltran-Mir, H.; Torres-Mendieta, R.; Andrés, J.; Oliva, M.; et al. Ag Nanoparticles/α-Ag$_2$WO$_4$ Composite Formed by Electron Beam and Femtosecond Irradiation as Potent Antifungal and Antitumor Agents. *Sci. Rep.* **2019**, *9*, 1–15. [CrossRef] [PubMed]

24. Assis, M.; Macedo, N.G.; Machado, T.R.; Ferrer, M.M.; Gouveia, A.F.; Cordoncillo, E.; Torres-Mendieta, R.; Beltrán-Mir, H.; Mínguez-Vega, G.; Leite, E.R.; et al. Laser/Electron Irradiation on Indium Phosphide (InP) Semiconductor: Promising Pathways to In Situ Formation of Indium Nanoparticles. *Part. Part. Syst. Charact.* **2018**, *35*, 1–10. [CrossRef]

25. Assis, M.; Cordoncillo, E.; Torres-Mendieta, R.; Beltrán-Mir, H.; Mínguez-Vega, G.; Gouveia, A.F.; Leite, E.; Andrés, J.; Longo, E. Laser-induced formation of bismuth nanoparticles. *Phys. Chem. Chem. Phys.* **2018**, *20*, 13693–13696. [CrossRef]

26. Añez, R.; Cabral, L.; da Silva, E.Z.; Longo, E.; Andrés, J.; San-Miguel, M.A. Unveiling the Ag-Bi miscibility at the atomic level: A theoretical insight. *Comput. Mater. Sci.* **2021**, *197*, 110612. [CrossRef]

27. Torres-Mendieta, R.O.; Teixeira, M.M.; Mínguez-Vega, G.; de Souza, D.; Gobato, Y.G.; Assis, M.; Longo, E. Toward Expanding the Optical Response of Ag2CrO4and Bi2O3by Their Laser-Mediated Heterojunction. *J. Phys. Chem. C* **2020**, *124*, 26404–26414. [CrossRef]

28. Ågren, R.; Zeberg, H. Low-Resistance silver bromide electrodes for recording fast ion channel kinetics under voltage clamp conditions. *J. Neurosci. Methods* **2020**, *348*, 108984. [CrossRef]

29. Thakur, P.; Raizada, P.; Singh, P.; Kumar, A.; Khan, A.A.P.; Asiri, A.M. Exploring recent advances in silver halides and graphitic carbon nitride-based photocatalyst for energy and environmental applications. *Arab. J. Chem.* **2020**, *13*, 8271–8300. [CrossRef]

30. Sharma, S.; Dutta, V.; Raizada, P.; Hosseini-Bandegharaei, A.; Thakur, V.K.; Kalia, S.; Nguyen, V.-H.; Singh, P. Recent advances in silver bromide-based Z-scheme photocatalytic systems for environmental and energy applications: A review. *J. Environ. Chem. Eng.* **2021**, *9*, 105157. [CrossRef]

31. Sambhy, V.; MacBride, M.M.; Peterson, B.R.; Sen, A. Silver bromide nanoparticle/polymer composites: Dual action tunable antimicrobial materials. *J. Am. Chem. Soc.* **2006**, *128*, 9798–9808. [CrossRef]

32. Perdew, J.P.; Burke, K.; Ernzerhof, M. Generalized gradient approximation made simple. *Phys. Rev. Lett.* **1996**, *77*, 3865. [CrossRef] [PubMed]

33. Blöchl, P.E. Projector augmented-wave method. *Matter Mater. Phys.* **1994**, *50*, 17953–17979. [CrossRef]

34. Joubert, D. From ultrasoft pseudopotentials to the projector augmented-wave method. *Phys. Rev. B Condens. Matter Mater Phys.* **1999**, *59*, 1758–1775.

35. Hafner, J. Materials simulations using VASP-a quantum perspective to materials science. *Comput. Phys. Commun.* **2007**, *177*, 6–13. [CrossRef]

36. Pizzi, G.; Vitale, V.; Arita, R.; Bluegel, S.; Freimuth, F.; Géranton, G.; Gibertini, M.; Gresch, D.; Johnson, C.; Koretsune, T.; et al. Wannier90 as a community code: New features and applications. *J. Physics Condens. Matter* **2019**, *32*, 165902. [CrossRef] [PubMed]

37. Ong, S.P.; Richards, W.D.; Jain, A.; Hautier, G.; Kocher, M.; Cholia, S.; Gunter, D.; Chevrier, V.L.; Persson, K.A.; Ceder, G. Python Materials Genomics (pymatgen): A robust, open-source python library for materials analysis. *Comput. Mater. Sci.* **2013**, *68*, 314–319. [CrossRef]

38. Wang, V.; Xu, N.; Liu, J.-C.; Tang, G.; Geng, W.-T. VASPKIT: A user-friendly interface facilitating high-throughput computing and analysis using VASP code. *Comput. Phys. Commun.* **2021**, *267*, 108033. [CrossRef]

39. Togo, A.; Tanaka, I. First principles phonon calculations in materials science. *Scr. Mater.* **2015**, *108*, 1–5. [CrossRef]

40. Kresse, G.; Hafner, J. Ab initio molecular dynamics for liquid metals. *Phys. Rev. B* **1993**, *47*, 558–561. [CrossRef]

41. Marzari, N.; Vanderbilt, D.; Payne, M.C. Ensemble density-functional theory for ab initio molecular dynamics of metals and finite-temperature insulators. *Phys. Rev. Lett.* **1997**, *79*, 1337–1340. [CrossRef]

42. Mermin, N.D. Thermal properties of the inhomogeneous electron gas. *Phys Rev.* **1965**, *137*, 1–3. [CrossRef]

43. Boukhtouta, M.; Lamraoui, S.; Touam, S.; Meradji, H.; Ghemid, S.; Hassan, F.E.H. Phase stability and electronic properties of silver halides. *Phase Transit.* **2015**, *88*, 357–367. [CrossRef]

44. Li, T.; Luo, S.; Yang, L. Microwave-assisted solvothermal synthesis of flower-like Ag/AgBr/BiOBr microspheres and their high efficient photocatalytic degradation for p-nitrophenol. *J. Solid State Chem.* **2013**, *206*, 308–316. [CrossRef]

45. Mouhat, F.; Coudert, F.-X. Necessary and sufficient elastic stability conditions in various crystal systems. *Phys. Rev. B* **2014**, *90*, 4–7. [CrossRef]

46. Ivlev, S.I.; Gaul, K.; Chen, M.; Karttunen, A.J.; Berger, R.; Kraus, F. Synthesis and Characterization of [Br 3][MF 6] (M=Sb, Ir), as well as Quantum Chemical Study of [Br 3] + Structure, Chemical Bonding, and Relativistic Effects Compared with [XBr 2] + (X=Br, I, At, Ts) and [TsZ 2] + (Z=F, Cl, Br, I, At, Ts). *Chem. A Eur. J.* **2019**, *25*, 5793–5802. [CrossRef]

47. Focsa, C.; Li, H.; Bernath, P. Characterization of the Ground State of Br2 by Laser-Induced Fluorescence Fourier Transform Spectroscopy of the B3Π0+u-X1Σ+g System. *J. Mol. Spectrosc.* **2000**, *200*, 104–119. [CrossRef]